nature nanotechnology

ARTICLES

https://doi.org/10.1038/s41565-021-01018-8

Nanoparticle cellular internalization is not required for RNA delivery to mature plant leaves

Huan Zhang[1,2,10], Natalie S. Goh[1,10], Jeffrey W. Wang[1], Rebecca L. Pinals[1], Eduardo González-Grandío[1], Gozde S. Demirer[1,3], Salwan Butrus[1], Sirine C. Fakra[4], Antonio Del Rio Flores[1], Rui Zhai[1], Bin Zhao[5], So-Jung Park[6] and Markita P. Landry[1,7,8,9] ✉

Rapidly growing interest in the nanoparticle-mediated delivery of DNA and RNA to plants requires a better understanding of how nanoparticles and their cargoes translocate in plant tissues and into plant cells. However, little is known about how the size and shape of nanoparticles influence transport in plants and the delivery efficiency of their cargoes, limiting the development of nanotechnology in plant systems. In this study we employed non-biolistically delivered DNA-modified gold nanoparticles (AuNPs) of various sizes (5–20 nm) and shapes (spheres and rods) to systematically investigate their transport following infiltration into *Nicotiana benthamiana* leaves. Generally, smaller AuNPs demonstrated more rapid, higher and longer-lasting levels of association with plant cell walls compared with larger AuNPs. We observed internalization of rod-shaped but not spherical AuNPs into plant cells, yet, surprisingly, 10 nm spherical AuNPs functionalized with small-interfering RNA (siRNA) were the most efficient at siRNA delivery and inducing gene silencing in mature plant leaves. These results indicate the importance of nanoparticle size in efficient biomolecule delivery and, counterintuitively, demonstrate that efficient cargo delivery is possible and potentially optimal in the absence of nanoparticle cellular internalization. Overall, our results highlight nanoparticle features of importance for transport within plant tissues, providing a mechanistic overview of how nanoparticles can be designed to achieve efficacious biocargo delivery for future developments in plant nanobiotechnology.

The growth of nanobiotechnology, whereby nanomaterials are designed for use in biological systems, has added new dimensionality to pharmaceutical and drug delivery development and married the fields of chemistry, biomedical engineering and material science. In recent years, the use of nanomaterials in plant science has greatly enabled agricultural advances. These developments include crop management improvement, plant pathogen protection, nutrient and pesticide delivery, monitoring of plant and soil health, and the creation of crop varieties with desirable traits such as high yield and stress resistance[1–3]. In plant genetic engineering, nanomaterials have also been used as vehicles for the delivery of plasmid DNA[4–6], short-interfering RNA (siRNA)[7–11] and proteins[12] to whole plants.

Nanoparticle (NP)-mediated biomolecule delivery technologies for plants have leveraged the material properties of nanoparticles to overcome the unique barriers of plant cells. Examples of these materials include mesoporous silica nanoparticles (MSNs)[4,12], single-walled carbon nanotubes (SWNTs)[5,6,8,13], DNA nanostructures[9], layered double hydroxide nanosheets[7,14] and, more recently, gold nanoparticles (AuNPs)[10,11]. These technologies exploit the small size and high tensile strength of NPs to bypass biological barriers. Moreover, the diverse conjugation chemistries available for cargo conjugation to NPs and the high degree of control over NP morphology and surface functionalization enable certain NPs to penetrate through plant tissues[15,16]. Although NP-mediated biomolecule delivery in plants has been demonstrated with nanoparticles of various sizes and surface modifications, little is known about how these design variables affect translocation, cellular uptake and ultimately biocargo utilization in plants. Comprehensive studies in mammalian systems[17–20] and simulations of NP–cell membrane interactions[21–24] have underscored the importance of NP size and shape for biodelivery, yet, these studies are usually not applicable to walled plant cells. In particular, studies in mammalian systems have revealed how size and shape can affect NP interaction with cells and thus influence the uptake pathway and internalization efficiency, guiding design strategies for nanoparticle-based biomedical applications[25]. However, analogous studies in plant systems have not yet been performed, limiting the development of plant nanobiotechnologies and the assessment of their intended and unintended impacts on plants, agricultural systems and the environment.

The plant cell wall is a complex network of biopolymers that gives rise to a semipermeable matrix[26] and is a unique barrier to consider for the uptake of NPs into plant cells[27]. Although cell wall permeability is dynamic, studies suggest that the upper limit of the pore diameters range from 5 to 20 nm[28,29]. The process of NP uptake, translocation and accumulation in plants can be broadly split into three tiers[30]: (1) the macroscale—quantifying translocation and accumulation in plant organs, (2) the microscale—studying NP transport through and interactions with plant tissues and vasculature, and (3) the molecular—revealing the manner of NP association on a cellular or subcellular level. Of note, most studies have been performed on the macroscale[31,32], although some have begun

[1]Department of Chemical and Biomolecular Engineering, University of California, Berkeley, Berkeley, CA, USA. [2]College of Chemistry and Materials Science, Jinan University, Guangzhou, China. [3]Department of Plant Biology and Genome Center, University of California, Davis, Davis, CA, USA. [4]Advanced Light Source, Lawrence Berkeley National Laboratory, Berkeley, CA, USA. [5]School of Biomedical Sciences and Engineering, South China University of Technology, Guangzhou, China. [6]Department of Chemistry and Nanoscience, Ewha Womans University, Seoul, Republic of Korea. [7]Innovative Genomics Institute, Berkeley, CA, USA. [8]California Institute for Quantitative Biosciences, University of California, Berkeley, Berkeley, CA, USA. [9]Chan Zuckerberg Biohub, San Francisco, CA, USA. [10]These authors contributed equally: Huan Zhang, Natalie S. Goh. ✉e-mail: landry@berkeley.edu

to explore the effect of NP properties on uptake at the microscale[15,33] and the molecular scale[34,35]. These studies are valuable to understand how NPs and their surface chemistries might impact translocation and long-term accumulation throughout a plant. However, NP features enabling molecular-scale translocation of NPs within plant tissues and into plant cells, and subsequent biocargo delivery, remain to be determined.

Although gold microparticles and certain larger AuNPs are broadly used for biolistic delivery of biological cargoes in plants, their non-biolistic delivery remains largely unexplored. In this study, we designed a library of DNA-functionalized gold nanoparticles (DNA-AuNPs) of varying sizes and shapes and evaluated their leaf tissue transport to plant cells over time. We used confocal microscopy, transmission electron microscopy (TEM) and synchrotron X-ray fluorescence (μXRF) imaging to track AuNP fate and directly visualize NP interactions with plant cells. Based on these results, we established a size- and shape-dependent mechanism of DNA-AuNP transport to and passage across plant cell walls and demonstrate here that biocargo delivery into plant cells can be independent of nanoparticle cellular internalization. Our results highlight the importance of nanoparticle morphology in transport within plant tissues and suggest that efficient cellular siRNA delivery can be achieved even without NP carrier internalization into cells.

Preparation and characterization of DNA-AuNPs

Five gold nanoparticles of various morphologies were used in this study: 5-, 10-, 15- and 20-nm-diameter gold nanospheres (AuNSs), and 13 nm × 68 nm gold nanorods (AuNRs) of aspect ratio ~5.2 (Fig. 1a). To obtain colloidally stable particles, the AuNPs were functionalized using a pH-assisted method[36] with single-stranded DNA sequences with a 3′-thiol modifier followed by a ten-nucleotide polyadenosine sequence (Supplementary Tables 1 and 2). Citrate-stabilized AuNPs and functionalized DNA-AuNPs were characterized by ultraviolet-visible-near-infrared (UV-Vis-NIR) spectroscopy, dynamic light scattering (DLS) and TEM imaging. The AuNSs exhibit a size-dependent surface plasmon resonance (SPR) peak at approximately 520 nm and the AuNRs show characteristic transverse and longitudinal peaks at 520 and 960 nm, respectively (Fig. 1b), with the SPR peaks showing small redshifts post-functionalization (Supplementary Fig. 1). DLS characterization (Supplementary Table 3 and Supplementary Figs. 2 and 3) and TEM (Fig. 1c and Supplementary Fig. 4) demonstrated successful functionalization and a high homogeneity of the AuNPs and DNA-AuNPs, and the number of DNA molecules per AuNP was quantified (Supplementary Table 4) with the AuNPs possessing higher surface areas loading more DNA, as expected. DNA-AuNPs were next tagged with the cyanine 3 (Cy3) fluorophore by complementary strand hybridization and abaxially infiltrated into mature leaves of *Nicotiana benthamiana* plants using a needleless syringe (Fig. 1d).

AuNP transport through leaf tissue and association with plant cells

Following nanoparticle characterization, we tested the morphology- and size-dependent ability of the AuNPs to transit within the leaf interstitial space and associate with plant cell walls. To track DNA-AuNPs in plant tissue, we hybridized a Cy3-modified complementary DNA strand to the thiol-modified DNA on AuNPs (Supplementary Table 1). The Cy3-labelled DNA-AuNPs (Cy3-DNA-AuNPs), with a normalized Cy3 concentration of 400 nM and thus differing concentrations of AuNP (Supplementary Table 4), were abaxially infiltrated into the leaves of a transgenic mGFP5 (a GFP variant) *N. benthamiana* plant. The leaves were adaxially (top) imaged by confocal microscopy to capture the Cy3 signal from the Cy3-DNA-AuNPs and the GFP signal from the transgenic *N. benthamiana* cytosol. The colocalization fraction between the Cy3 and GFP channels represents the relative ability of Cy3-DNA-AuNPs to diffuse within the leaf interstitial space and associate with (and/or enter, see Supplementary Note 1) plant cells (Fig. 2a).

Colocalization analyses of Cy3-DNA-AuNPs with cytosolic mGFP5 30 min to 24 h post-infiltration revealed maximum colocalization fractions at varying timepoints that depend on AuNP core shape and size (Fig. 2b, maxima: black bars), with the exception of 20 nm AuNSs, for which no maximum was observed. The confocal images in Fig. 2c show the Cy3-DNA-AuNP signal as the red channel, intracellular GFP as the green channel and the colocalization signal from the two channels in white. With the exception of the 20 nm AuNSs, all DNA-AuNPs experienced an increase in colocalization fractions as a function of time post-infiltration before reaching a maximum, followed by a decrease in colocalization values over longer incubation times (Supplementary Figs. 5–9). For the DNA-AuNSs, the time required to reach maximum AuNP colocalization with plant cells was faster for smaller nanoparticles: for 5, 10 and 15 nm DNA-AnNSs, the times corresponding to the colocalization maxima were 1, 2 and 12 h post-infiltration. For 20 nm DNA-AuNSs, no statistically significant change in the colocalization fractions occurred within 24 h, and longer post-infiltration times of 48 and 72 h did not yield a maximum value. For the DNA-AuNRs, the maximum colocalization fraction occurred sharply at 6 h post-infiltration.

We attribute the time-dependent increase in the colocalization fraction to the time required for DNA-AuNPs to travel through plant tissue and intercalate between cells. Interestingly, the different time-dependent accumulation of DNA-AuNSs compared with DNA-AuNRs suggests a shape-dependent effect on NP transport in plant tissues. Additional confocal experiments with a lower aspect ratio AuNR support this hypothesis (Supplementary Discussion 1 and Supplementary Figs. 10 and 11). The decrease in the Cy3 signal at longer incubation times is potentially due to the loss of Cy3 fluorescence through photobleaching or quenching by molecular interactions[37], or apoplastic[38] (space beyond the cell plasma membrane) transport decreasing the Cy3 presence within the imaged area (Supplementary Discussion 2 and Supplementary Figs. 12 and 13). Altogether, our data suggest that AuNS core size plays an essential role in DNA-AuNP transport in plant tissues: 5, 10 and 15 nm DNA-AuNSs and DNA-AuNRs with diameters less than 15 nm can diffuse within the leaf interstitial space and associate with plant cell walls and membranes in a size- and shape-dependent manner, with times for maximal cellular association ranging drastically from 1 to 12 h. These findings support prior observations that larger NPs take longer to diffuse through plant tissue and associate with plant cells, with an upper NP core size limit 20 nm (ref. [12]).

Visualization of AuNS association with plant leaf cells

To confirm the fate of NPs on a subcellular scale, we next performed TEM on NP-treated leaves to directly visualize the AuNPs in plants (Fig. 3). DNA-AuNP-infiltrated *N. benthamiana* leaves were fixed and sectioned 24 h post-infiltration prior to imaging. Figure 3a–d shows progressively increased magnifications for 5, 10, 15 and 20 nm AuNSs, with arrows marking the AuNSs associated with a single cell wall and unfilled arrows marking AuNSs sandwiched between two neighbouring cell walls (Supplementary Table 4). Characteristic cellular structures such as chloroplasts and cell walls have been used as indicators to determine whether AuNSs are localized within the extracellular or intracellular spaces.

Across all samples, we observed a high density of AuNSs associated with plant cell walls, with smaller AuNSs associating more than larger AuNSs. Our colocalization analysis demonstrated that the size of the AuNSs affects their translocation efficiency within plant tissues, whereby larger AuNS experience greater difficulty bypassing biological barriers. Notably, the 5, 10 and 15 nm DNA-AuNS TEM images showed AuNSs intercalating into a single cell wall, whereas

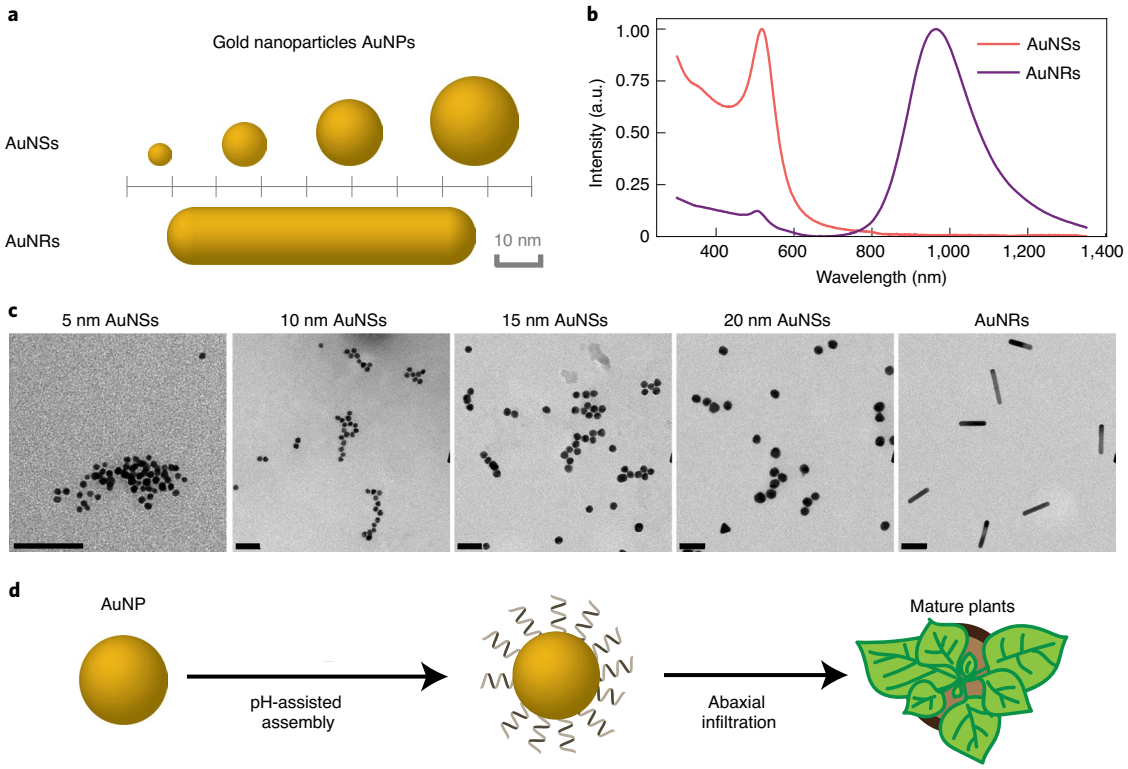

Fig. 1 | DNA-AuNP preparation and characterization. a, AuNP samples used in this study: 5-, 10-, 15- and 20-nm-diameter AuNSs, and 13 nm × 68 nm AuNRs. **b**, Representative UV-Vis-NIR spectra of 10 nm AuNSs and the AuNRs demonstrate characteristic AuNS and AuNR absorbance peaks. **c**, TEM characterization of the AuNPs indicates a high degree of monodispersity. Scale bars, 50 nm. **d**, AuNPs were functionalized with thiol-modified nucleic acids by a low-pH-assisted method, followed by abaxial infiltration into mature plant leaves. Throughout this study, infiltration was performed in lieu of spray-based nanoparticle application to ensure even wetting of the plant leaf tissue.

the 20 nm AuNS images depicted AuNSs sandwiched between two cell walls and thus unassociated with a single cell (Fig. 3d and Supplementary Fig. 16). Across all samples, we saw no instances of AuNSs within or proximal to the intracellular space of plant cells, suggesting that AuNS internalization into plant cells is minimal, if it occurs at all (additional confirmation is presented in Supplementary Fig. 17). The higher degree of plant leaf cell association of smaller AuNPs based on TEM agrees with their respective higher colocalization values obtained by our confocal microscopy analysis.

Visualization of AuNR association with and internalization into plant leaf cells

Analogous to the AuNS TEM experiments, *N. benthamiana* leaves exposed to DNA-AuNRs were prepared for TEM analysis 24 h post-infiltration. In contrast to AuNS, we identified several AuNRs inside plant cells (Fig. 4a). The striped arrow pinpoints a AuNR found within a plant cell, supported by the presence of chloroplasts next to the identified AuNR. In addition, several instances of AuNRs piercing into cell walls were observed, orienting along a tangent or perpendicular to the cell wall (Fig. 4b and Supplementary Fig. 18).

Previous theoretical and experimental studies of NP internalization into mammalian cells indicated that NP shape greatly influences the contact curvature with the lipid membrane and dictates the endocytic pathway and angle of entry[22]. In particular, high-aspect ratio NPs tend to rotate to orient themselves perpendicular to the cell membrane during internalization into mammalian cells[21], whereby the rotation facilitates the penetration and transport of the NPs[39]. From our TEM data, we therefore analysed AuNRs in the extracellular space of plant cells with respect to their orientation relative to the cell wall tangent (Fig. 4c and Supplementary Fig. 19). In total, 41.7%, 21.9% and 36.4% of AuNRs oriented in ranges of 0–30°, 30–60° and 60–90° with respect to the cell wall, respectively (Supplementary Fig. 19 and Supplementary Table 5). We posit that the AuNRs demonstrate a stronger preference for initially orienting parallel to the cell wall, where 22.5% of AuNRs form an acute angle of 0–10° with the cell wall. In addition, compared with the 11.1% proportion expected randomly (Supplementary Statistics and Data Analysis and Supplementary Table 5), 14.2% of AuNRs were oriented at 80–90° relative to the plane of the cell wall. Considering the rigid and porous structure of the cell wall, we posit that AuNRs experience reorientation to bypass the cell wall and membrane for plant cell internalization, similar to the phenomenon previously identified in mammalian systems, suggesting that asymmetric nanoparticles are entropically favoured for membrane interactions[21,22,39].

To further verify the importance of AuNP morphology in transport through plant leaf tissues, we performed μXRF mapping of cross-sections of DNA-AuNP (10 and 20 nm DNA-AuNS and DNA-AuNR)-infiltrated wild-type (WT) *N. benthamiana* leaves prepared 24 h post-infiltration. Comparing with a water-infiltrated control (Supplementary Fig. 20), all AuNP samples showed the Au signal throughout the leaf cross-section (Fig. 4d). μXRF mapping confirmed that the transport of 20 nm DNA-AuNPs through leaf tissue is size-limited, limiting their transport past the leaf cuticle or initial layer of epidermal cells (Supplementary Figs. 21 and 22). In comparison, smaller 10 nm DNA-AuNSs and DNA-AuNRs demonstrated highly homogeneous transport within the leaf cross-section, as seen from consistent Au counts throughout the leaf's full thickness (Supplementary Figs. 23–26).

Hypothesized mechanisms for NP internalization into plant cells include endocytosis, entry through the plasmodesmata and NPs acting as 'nanospears' to 'pierce' membranes[39]. To better understand

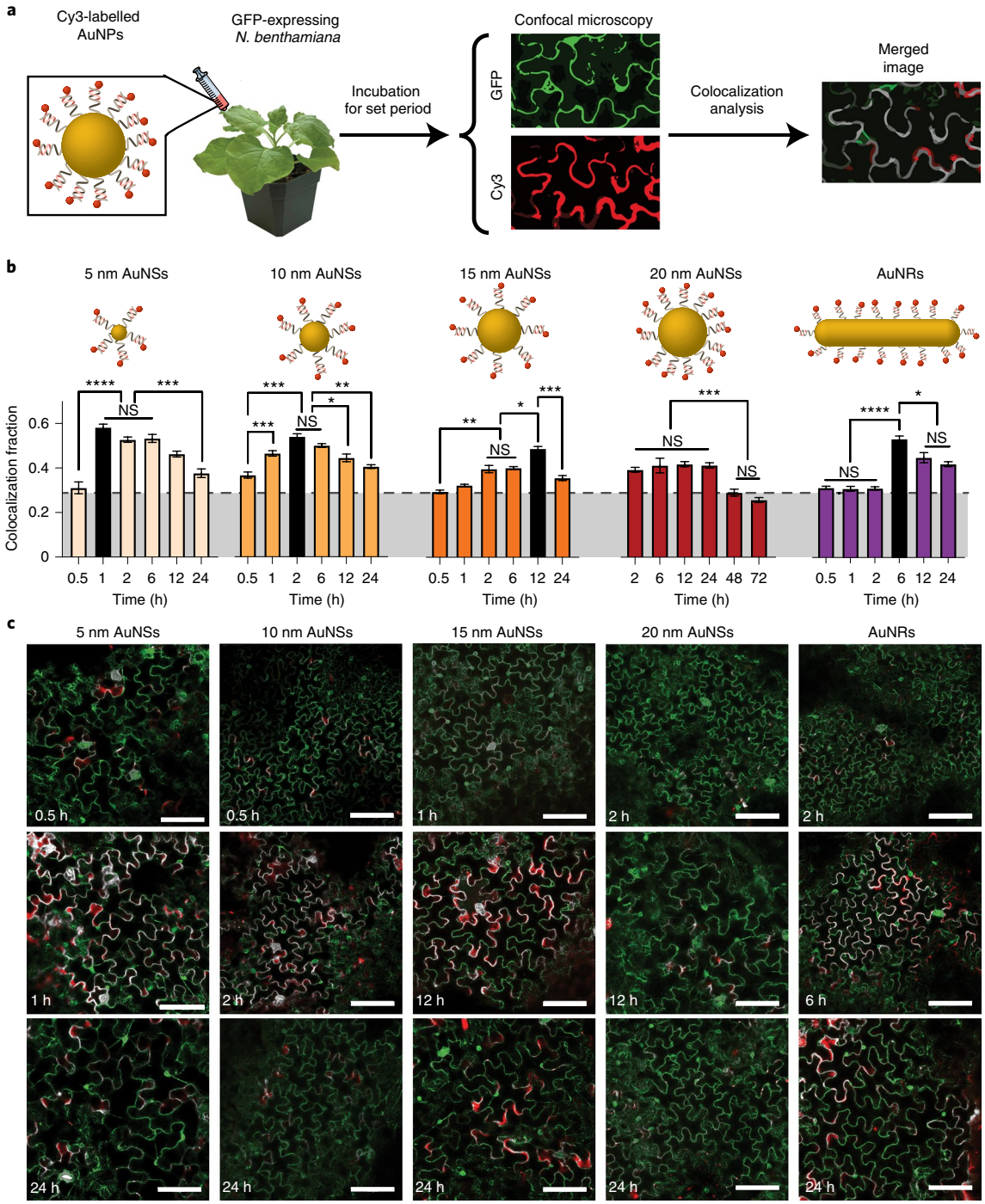

Fig. 2 | Cy3-tagged DNA-AuNP association with plant cells following infiltration into transgenic mGFP5 *N. benthamiana* leaves. a, Workflow for fluorescent AuNP tracking in leaves by confocal microscopy. AuNPs labelled with 400 nM Cy3-DNA abaxially infiltrated into mGFP5 *N. benthamiana* leaves (with GFP fluorescence as a cytosolic marker) and colocalization fractions analysed by confocal microscopy as a relative measure of AuNP cell wall association. **b**, Time series of colocalization fractions of Cy3-DNA-AuNPs demonstrate size- and shape-dependent AuNP transport in plant tissues. The horizontal dashed line denotes the maximum colocalization fractions obtained with a free Cy3-DNA control (Supplementary Figs. 14 and 15**)**. 5 nm AuNS: $^{****}P<0.0001$, $^{***}P=0.0008$; 10 nm AuNS: $^{***}P=0.0003$, $^{**}P=0.0030$, $^{*}P=0.0357$; 15 nm AuNS: $^{***}P=0.0009$, $^{**}P=0.0056$, $^{*}P=0.0276$; 20 nm AuNS: $^{***}P=0.0004$; AuNR: $^{****}P<0.0001$, $^{*}P=0.0115$ by one-way analysis of variance (ANOVA); NS, not significant. The error bars indicate s.e.m. ($n=3$). **c**, Cy3-DNA-AuNP-infiltrated *N. benthamiana* leaves with regions of colocalization (white) between intracellular GFP (green) and Cy3 (red) channels. Images are shown for each of the five AuNP samples at incubation times corresponding to before, during and after the time for the colocalization values to reach the maximum level. Scale bars, 100 μm.

AuNR plant cell internalization, we assessed the impact of endocytosis inhibition on Cy3-DNA-AuNP association with plant cells using confocal microscopy. We infiltrated the leaves of mGFP5 *N. benthamiana* with endocytosis inhibitors (either wortmannin[40] or ikarugamycin[41]), then infiltrated the same area with Cy3-DNA-AuNPs (10 nm AuNSs or AuNRs) 30 min later.

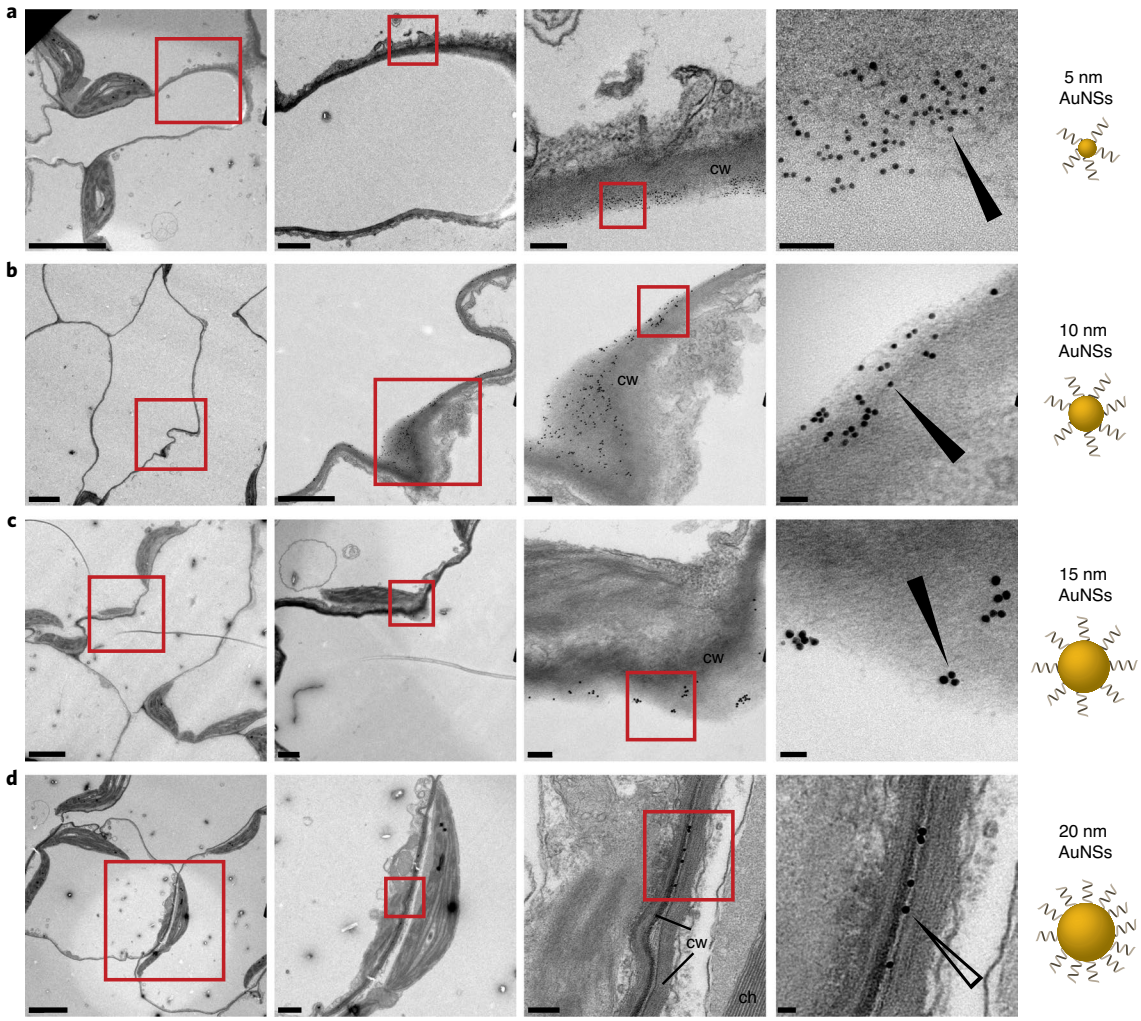

Fig. 3 | TEM of DNA-functionalized AuNS-treated *N. benthamiana* leaves. a–d, Representative TEM images of *N. benthamiana* plants 24 h post-infiltration with DNA-functionalized AuNSs with diameters of 5 nm (**a**), 10 nm (**b**), 15 nm (**c**) and 20 nm (**d**). The images show progressive magnifications from left to right, with the red boxes indicating the areas of magnification. Annotations represent cell wall (cw) and chloroplast (ch). The filled and open arrows indicate nanoparticles associated with a single cell wall or found between cell walls, respectively. Scale bars from left to right, 5 µm, 1 µm, 0.2 µm and 50 nm.

Colocalization analysis was performed 6 h post-AuNP infiltration by normalizing the values for samples treated with endocytosis inhibitors to controls without inhibitors.

As shown in Fig. 4e, samples pretreated with either wortmannin or ikarugamycin endocytosis inhibitor induced a marked decrease in colocalization fraction for AuNRs, but no significant change was observed for 10 nm AuNSs (Supplementary Fig. 27). Wortmannin is an inhibitor of phosphoinositol-3 kinase activity and disrupts protein transport to vacuoles[40,42]. Although the mechanism of action of ikarugamycin is undetermined, it is often used as an inhibitor of clathrin-mediated endocytosis[41,43]. Despite their different modes of action on plant cell trafficking, both wortmannin and ikarugamycin inhibit the entry of Cy3-DNA-AuNRs, whereas neither affects the colocalization values of 10 nm Cy3-DNA-AuNSs with the plant cell cytosol. These experiments, which were based on a disruption of the plant cell's native endocytic pathways, together with our TEM results suggest that AuNRs do internalize into plant cells through energy-dependent mechanisms whereas AuNSs do not internalize into plant cells.

Based on these findings, we propose a mechanism of AuNP transport within plant leaf tissues (Fig. 4f). Briefly, upon introduction to mature plant leaves, both DNA-AuNSs and DNA-AuNRs transport to the periphery of plant cells in a size-dependent manner and experience a high degree of association with the cell wall. While AuNSs cannot bypass the cell wall, AuNRs may orient in parallel to the cell wall during initial contact and reorient perpendicularly when bypassing the cell wall, which supports the proposed mechanisms of rotation-based cell wall entry of rod-shaped nanomaterials[21,39]. After passage through the cell wall, endocytosis is a likely mechanism of AuNR entry across the cell membrane.

Sub-20 nm AuNPs enable delivery of siRNA for gene silencing in mGFP5 *N. benthamiana* plants

Targeted downregulation of certain plant proteins is known to confer disease resistance in crops. Therefore, an attractive 'greener' alternative to the use of herbicides in agriculture is RNA interference, which involves the delivery of siRNA molecules that interfere with the production of a specific plant protein. However, siRNA is a molecule that is difficult to deliver across the cell wall due to its high susceptibility to degradation[44,45]. We therefore evaluated the use of AuNPs as delivery vehicles to enable transient gene silencing through siRNA delivery into *N. benthamiana* leaves. AuNP samples of varying morphologies and sizes were functionalized with prehybridized siRNA targeting the *GFP* gene to obtain siRNA-functionalized AuNPs

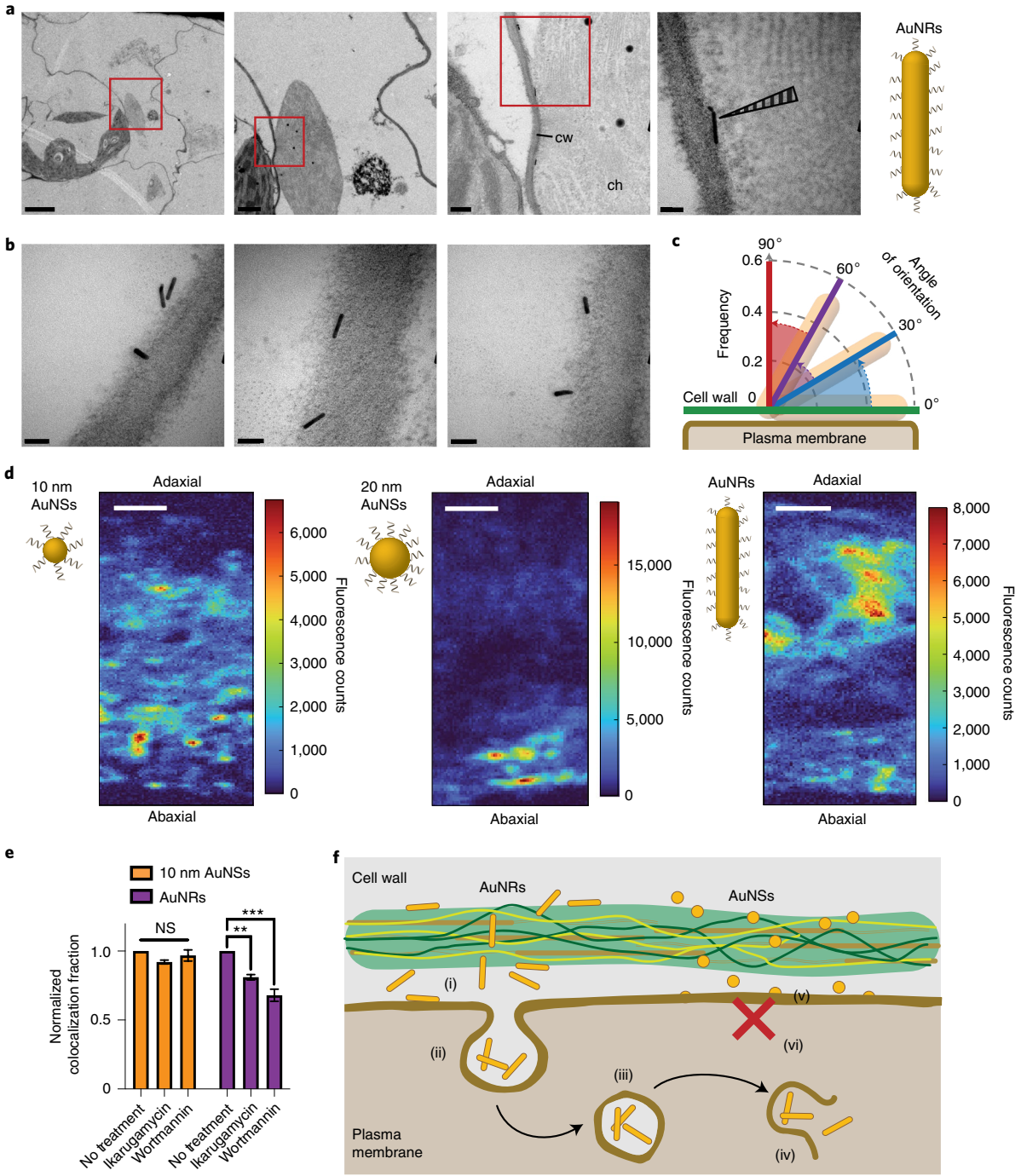

Fig. 4 | TEM and μXRF imaging of DNA-AuNP-treated *N. benthamiana* leaves and mechanism of morphology-dependent AuNP transport. a, TEM images of *N. benthamiana* plants 24 h post-infiltration with DNA-functionalized AuNRs. Annotations represent cell wall (cw) and chloroplast (ch). Scale bars from left to right, 5 μm, 1 μm, 0.2 μm and 50 nm. **b**, AuNRs exhibit a variety of orientations upon contact with the cell wall, including AuNRs 'piercing' the cell wall, a potential mode of NP internalization. Scale bars, 50 nm. **c**, Proportion of AuNRs observed within an angle range depicted by the shaded radial magnitude slices. The statistical analysis shows that AuNR orientation maximizes contact area with the cell wall (0–30°) and minimizes orientations perpendicular to the cell wall (60–90°) for $n = 324$ AuNRs (Supplementary Table 5). **d**, μXRF Au distribution map of *N. benthamiana* leaf cross-section exposed to 5 μg of 10 and 20 nm DNA-AuNSs and DNA-AuNRs. The intensity values correspond to Au $L\alpha_1$ fluorescence emission counts. All maps are positioned with the abaxial side facing down (side of infiltration). Scale bars, 50 μm. **e**, Colocalization fractions between Cy3 and GFP channels for Cy3-tagged DNA-functionalized 10 nm AuNSs and AuNRs infiltrated into mGFP5 *N. benthamiana* leaves treated with endocytosis inhibitors ikarugamycin or wortmannin. No change in colocalization fraction values was observed with AuNSs, although AuNR samples in leaves treated with ikarugamycin or wortmannin demonstrated a significant decrease in colocalization fractions normalized to untreated samples. AuNR: $^{**}P = 0.007$, $^{***}P = 0.0005$ by two-way ANOVA. The error bars indicate s.e.m. ($n = 3$). **f**, Mechanistic schematic for AuNS and AuNR association or internalization into plant cells. AuNRs may orient on their long ends to 'pierce' cell walls (i). AuNRs found in intact plant cells likely enter through endocytosis (ii)–(iv). AuNSs show high association with the cell wall (v), but no instances of any sized AuNS were identified inside plant cells within 24 h (vi).

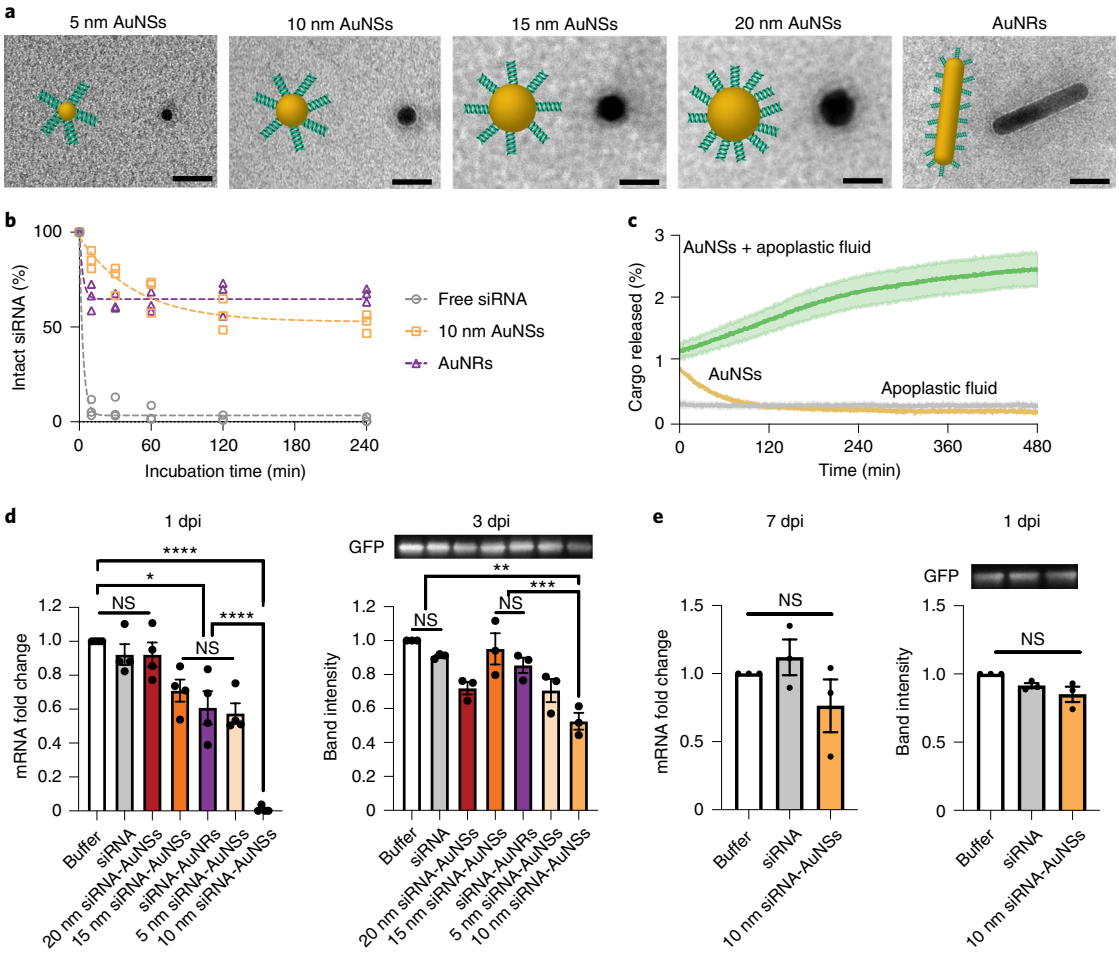

Fig. 5 | Size- and morphology-dependent siRNA-AuNP delivery in mGFP5 *N. benthamiana* leaves. a, TEM images of stained siRNA-functionalized AuNPs. Scale bars, 20 nm. **b**, AuNPs protect siRNA from endoribonuclease RNase A degradation. siRNA-loaded 10 nm AuNSs and AuNRs were incubated with RNase A for 10, 30, 60, 120 and 240 min prior to the quantification of intact siRNA. **c**, Fluorophore-tagged cargo desorbs from the AuNS surface in the presence of apoplastic fluid (green) with negative controls of 0.3× phosphate-buffered saline (PBS) added to TR-DNA-AuNSs (yellow) and apoplastic fluid alone (grey). The shaded error bars indicate s.e.m. ($n=2$). **d**, RT–qPCR (left) and western blot (right) quantification of GFP mRNA fold change and protein expression 1 and 3 days post-infiltration (dpi), respectively, of mGFP5 *N. benthamiana* plant leaves treated with siRNA-AuNPs loaded with 100 nM siRNA. RT–qPCR: $^{*}P=0.0411$, $^{****}P<0.0001$ in one-way ANOVA on day 1. The error bars indicate s.e.m. ($n=4$). Western blot: $^{**}P=0.0020$, $^{***}P=0.0074$ in one-way ANOVA on day 3. The error bars indicate s.e.m. ($n=3$). **e**, RT–qPCR (left) and western blot (right) analyses showing that GFP mRNA and protein expression levels, respectively, return to baseline 7 dpi with siRNA-AuNPs in *N. benthamiana* leaves. The buffer controls represent 0.3× PBS-infiltrated leaves. RT–qPCR: one-way ANOVA on day 7. The error bars indicate s.e.m. ($n=3$). Western blot: one-way ANOVA on day 7. The error bars indicate s.e.m. ($n=3$).

(siRNA-AuNPs; Supplementary Tables 1, 2 and 4). In addition to UV-Vis-NIR (Supplementary Fig. 1) and DLS characterization (Supplementary Fig. 28), uranium-based staining of siRNA-AuNPs in TEM analysis showed a visible halo surrounding the AuNPs, suggesting successful siRNA functionalization (Fig. 5a).

Prior to siRNA delivery in plants, we conducted in vitro experiments to probe the ability of AuNPs to protect siRNA. Following incubation with a high concentration of RNase A (1.2 μg ml^{-1}), nuclease inactivation and siRNA liberation from the AuNP surface, we quantified the concentration of remaining siRNA. Whereas free siRNA demonstrated extreme susceptibility to endonuclease degradation, a strong protective effect was afforded by the 10 nm AuNSs and AuNRs (Fig. 5b and Supplementary Table 6). Free siRNA degraded within 10 min of endonuclease exposure (7 ± 4% remaining), whereas 10 nm AuNSs and AuNRs exhibited 54 ± 5% and 64 ± 6% intact siRNA by 240 min. We further confirmed that AuNSs of all sizes, that is, 5, 10, 15 and 20 nm AuNSs, provide substantial protection against siRNA endonuclease degradation (Supplementary Fig. 29).

Next, we investigated the possibility of siRNA delivery using AuNP carriers even without nanoparticle internalization in plant cells. We tested siRNA bioavailability by measuring the RNA released from siRNA-AuNP-infiltrated leaves using anion-exchange fast protein liquid chromatography (FPLC)[46] and agarose gel electrophoresis, which both confirmed that siRNA becomes bioavailable following infiltration into plant leaves (Supplementary Figs. 30 and 31). We further verified that siRNA is liberated from siRNA-AuNPs in plant biofluids (both apoplastic fluid and plant lysate), and that this result is consistent across all AuNPs, by a gel-based assay (Supplementary Figs. 32 and 33). These results confirm that siRNA can be liberated from the AuNP surface in the extracellular or intracellular environment of the plant, and are noteworthy because they confirm that siRNA-AuNPs in the apoplast are protected against nuclease degradation and that siRNA can become

bioavailable proximal to the cell wall. To explore the mechanism of nucleic acid release from AuNPs, we used a fluorescence-based dynamic exchange assay[47] (Supplementary Fig. 34) to track cargo release from the AuNPs. We incubated 15 nm AuNSs conjugated with Texas red fluorophore-labelled DNA (TR-DNA-AuNS) with plant apoplastic fluid, which resulted in TR-DNA cargo release from the AuNS surface over time (Fig. 5c). Additionally, pH variation and the presence of the reactive oxidative species (ROS) H_2O_2 did not result in significant TR-DNA desorption (Supplementary Fig. 35), suggesting that neither the dynamic pH within the apoplast[48] (pH ≈ 6) nor an increase in ROS, commonly implicated with plant mechanical and environmental stress[49,50], are major contributing factors to cargo availability from the AuNSs. These experiments demonstrate that cargo loaded onto AuNSs located in the apoplast can desorb from the AuNP carrier, making the siRNA bioavailable, through a surface exchange mechanism involving cargo displacement due to biomolecule adsorption on the AuNS surface (Supplementary Note 2).

GFP-targeting siRNA-AuNPs were next infiltrated into GFP-expressing *N. benthamiana* leaves at a normalized siRNA concentration of 100 nM as previously used[8]. We extracted messenger RNA (mRNA) and protein from treated leaf tissue and quantified the efficiency of *GFP* silencing at the mRNA level 1 day post-infiltration (dpi) by means of quantitative PCR with reverse transcription (RT–qPCR) and protein-level *GFP* silencing 3 dpi by the western blot technique (Fig. 5d). We initially hypothesized that only AuNRs would enable efficient siRNA delivery and *GFP* silencing, because only AuNRs were found to enter plant cells within the timescale of our experiments. Surprisingly, we observed *GFP* silencing with both AuNSs and AuNRs, with smaller AuNSs generally more effective at silencing than larger AuNSs: 10 nm AuNSs showed the greatest amount of silencing across all AuNPs at both the mRNA (99%) and protein (48%) levels. The reductions in *GFP* mRNA transcripts 1 dpi were 8% (free siRNA), 8% (20 nm AuNSs), 29% (15 nm AuNSs), 39% (AuNRs), 42% (5 nm AuNSs) and 99% (10 nm AuNSs; Fig. 5c and Supplementary Fig. 36). Similarly, we measured a concomitant reduction in protein levels on 3 dpi (Fig. 5d and Supplementary Discussion 3). We also confirmed that gene silencing was transient by RT–qPCR and Western blot analyses of 10 nm siRNA-AuNS-infiltrated leaves 7 dpi (Fig. 5e), with the mRNA and protein levels returning to untreated control baseline several days after treatment. We next confirmed that *GFP* gene silencing was specific to the *GFP*-targeting siRNA sequence: RT–qPCR analysis of nonsense siRNA-functionalized 10 nm AuNSs at 1 dpi showed no silencing of the *GFP* gene, as expected (Supplementary Fig. 37). Taken together with our findings that apoplastic fluid constituents can induce siRNA desorption from AuNPs, these results stand in contrast to the assumption that NP cellular internalization is required for biomolecular cargo delivery for certain AuNP shapes and sizes. Specifically, our results suggest that the internalization of NPs is not necessary for efficient siRNA delivery and gene silencing in plants.

Lastly, we confirmed the biocompatibility of nucleic acid (NA)-functionalized AuNP constructs. To our knowledge, the biocompatibility of NA-functionalized AuNPs in plants has not been studied. To gauge the response of *N. benthamiana* to NA-functionalized AuNPs, we infiltrated *N. benthamiana* leaves with either buffer or AuNPs and performed a RT–qPCR analysis of the mRNA transcript levels for 13 genes associated with various stress responses (Supplementary Tables 1, 4 and 7, and Supplementary Note 3). We sampled leaves at various timepoints to study the effect of the infiltration itself compared with the effect of the AuNPs (10 nm AuNSs). The results in Supplementary Fig. 38 show the upregulation of several stress-related genes for both citrate-stabilized AuNSs and siRNA-AuNSs immediately post-infiltration, which returned to basal expression levels at 1 dpi. We further confirmed the recovery to baseline levels of gene expression by probing at 1 dpi the respiratory burst oxidase homologue B (*NbrbohB*) stress gene with 10 nm siRNA-AuNSs and siRNA-AuNRs (Supplementary Fig. 39). The results show that neither caused any significant change in *NbrbohB* gene expression. Additionally, a visual observation of leaves infiltrated with AuNPs immediately and at 3 dpi revealed no visible morphological changes (Supplementary Fig. 40). Taken together, these results suggest any stress response to AuNPs is transient and unlikely to result in physiological changes, suggesting that AuNPs can serve as biocompatible siRNA delivery vehicles to plants.

Conclusion

We systematically employed a series of DNA-AuNPs of various size (5–20 nm) and shape (spheres and rods) to investigate how morphology impacts nanoparticle interaction with and uptake into plant cells following infiltration into mature *N. benthamiana* leaves. We found that smaller AuNSs associate with plant cell walls faster than their larger counterparts, with a plant cell wall size exclusion limit of ~20 nm (refs. [28,29]). Our assays further revealed that although sub-20 nm AuNPs associate with plant cell walls, no AuNSs of any size enters plant cells. Interestingly, we found that AuNRs do enter plant cells, despite having a smallest dimension similar to the 10 nm AuNSs studied. Lastly, mechanistic studies alluded to endocytosis as a major contributor to AuNR internalization into plant cells.

Our findings suggest that smaller nanoparticles such as our 5, 10 and 15 nm AuNSs experience greater freedom of movement in convective flows within leaf tissues and are thus more easily transported to individual cell walls. Separately, the analysis of hundreds of AuNRs suggests that rods may translocate across the plant cell wall through a rotation-mediated process that positions rods favourably at acute angles with respect to the plane of the cell wall.

We lastly demonstrated that siRNA-loaded AuNPs below 20 nm enable silencing of a GFP transgene. Interestingly, gene silencing was accomplished by all sub-20 nm AuNSs despite their lack of cell internalization. We achieved the highest efficiency (99%) of gene silencing with non-cell-internalizing 10 nm siRNA-loaded AuNSs. We hypothesize that the interaction of the AuNPs with individual plant cell walls increases their residence time proximal to cells, providing more opportunity for siRNA permeation into and utilization by plant cells. Cell wall-associated AuNPs act as reservoirs for siRNA, releasing siRNA from the gold surface upon exchange with biomolecules in the surrounding biofluids whilst simultaneously protecting the siRNA cargo from nuclease degradation (Supplementary Fig. 41). These findings underscore our conclusion that although AuNPs do not need to enter cells to deliver their cargoes, AuNPs must intercalate into the plant cell wall for their cargoes to be efficiently utilized: it is insufficient for AuNPs to reside between cells for cargo delivery. These unintuitive shape- and size-dependent transport, internalization and silencing efficiencies of NA-functionalized AuNPs motivate a non-canonical approach to the development of future plant nanobiotechnologies, including the rational design of AuNPs for the delivery of various payloads such as mRNA and protein to advance plant biotechnology and agriculture.

Online content

Any methods, additional references, Nature Research reporting summaries, source data, extended data, supplementary information, acknowledgements, peer review information; details of author contributions and competing interests; and statements of data and code availability are available at https://doi.org/10.1038/s41565-021-01018-8.

Received: 17 March 2021; Accepted: 27 September 2021;
Published online: 22 November 2021

References

1. Liu, Y. et al. A gene cluster encoding lectin receptor kinases confers broad-spectrum and durable insect resistance in rice. *Nat. Biotechnol.* **33**, 301–305 (2015).
2. Li, T., Liu, B., Spalding, M. H., Weeks, D. P. & Yang, B. High-efficiency TALEN-based gene editing produces disease-resistant rice. *Nat. Biotechnol.* **30**, 390–392 (2012).
3. Karny, A., Zinger, A., Kajal, A., Shainsky-Roitman, J. & Schroeder, A. Therapeutic nanoparticles penetrate leaves and deliver nutrients to agricultural crops. *Sci. Rep.* **8**, 7589 (2018).
4. Torney, F., Trewyn, B. G., Lin, V. S. Y. & Wang, K. Mesoporous silica nanoparticles deliver DNA and chemicals into plants. *Nat. Nanotechnol.* **2**, 295–300 (2007).
5. Demirer, G. S. et al. High aspect ratio nanomaterials enable delivery of functional genetic material without DNA integration in mature plants. *Nat. Nanotechnol.* **14**, 456–464 (2019).
6. Kwak, S.-Y. et al. Chloroplast-selective gene delivery and expression in planta using chitosan-complexed single-walled carbon nanotube carriers. *Nat. Nanotechnol.* **14**, 447–455 (2019).
7. Mitter, N. et al. Clay nanosheets for topical delivery of RNAi for sustained protection against plant viruses. *Nat. Plants* **3**, 16207 (2017).
8. Demirer, G. S. et al. Carbon nanocarriers deliver siRNA to intact plant cells for efficient gene knockdown. *Sci. Adv.* **6**, eaaz0495 (2020).
9. Zhang, H. et al. DNA nanostructures coordinate gene silencing in mature plants. *Proc. Natl Acad. Sci. USA* **116**, 7543 (2019).
10. Lei, W.-X. et al. Construction of gold-siRNA$_{NPR1}$ nanoparticles for effective and quick silencing of *NPR1* in *Arabidopsis thaliana*. *RSC Adv.* **10**, 19300–19308 (2020).
11. Zhang, H. et al. Gold-nanocluster-mediated delivery of siRNA to intact plant cells for efficient gene knockdown. *Nano Lett.* https://doi.org/10.1021/acs.nanolett.1c01792 (2021).
12. Martin-Ortigosa, S. et al. Mesoporous silica nanoparticle-mediated intracellular Cre protein delivery for maize genome editing via *loxP* site excision. *Plant Physiol.* **164**, 537–547 (2014).
13. Liu, Q. et al. Carbon nanotubes as molecular transporters for walled plant cells. *Nano Lett.* **9**, 1007–1010 (2009).
14. Bao, W., Wang, J., Wang, Q., O'Hare, D. & Wan, Y. Layered double hydroxide nanotransporter for molecule delivery to intact plant cells. *Sci. Rep.* **6**, 26738 (2016).
15. Avellan, A. et al. Nanoparticle size and coating chemistry control foliar uptake pathways, translocation, and leaf-to-rhizosphere transport in wheat. *ACS Nano* **13**, 5291–5305 (2019).
16. Spielman-Sun, E. et al. Protein coating composition targets nanoparticles to leaf stomata and trichomes. *Nanoscale* **12**, 3630–3636 (2020).
17. Zhang, S., Gao, H. & Bao, G. Physical principles of nanoparticle cellular endocytosis. *ACS Nano* **9**, 8655–8671 (2015).
18. Herd, H. et al. Nanoparticle geometry and surface orientation influence mode of cellular uptake. *ACS Nano* **7**, 1961–1973 (2013).
19. Xie, X., Liao, J., Shao, X., Li, Q. & Lin, Y. The effect of shape on cellular uptake of gold nanoparticles in the forms of stars, rods, and triangles. *Sci. Rep.* **7**, 3827 (2017).
20. Chithrani, B. D., Ghazani, A. A. & Chan, W. C. W. Determining the size and shape dependence of gold nanoparticle uptake into mammalian cells. *Nano Lett.* **6**, 662–668 (2006).
21. Yi, X., Shi, X. & Gao, H. A universal law for cell uptake of one-dimensional nanomaterials. *Nano Lett.* **14**, 1049–1055 (2014).
22. Huang, C., Zhang, Y., Yuan, H., Gao, H. & Zhang, S. Role of nanoparticle geometry in endocytosis: laying down to stand up. *Nano Lett.* **13**, 4546–4550 (2013).
23. Shi, X., von dem Bussche, A., Hurt, R. H., Kane, A. B. & Gao, H. Cell entry of one-dimensional nanomaterials occurs by tip recognition and rotation. *Nat. Nanotechnol.* **6**, 714–719 (2011).
24. Vácha, R., Martinez-Veracoechea, F. J. & Frenkel, D. Receptor-mediated endocytosis of nanoparticles of various shapes. *Nano Lett.* **11**, 5391–5395 (2011).
25. Hui, Y. et al. Role of nanoparticle mechanical properties in cancer drug delivery. *ACS Nano* **13**, 7410–7424 (2019).
26. Houston, K., Tucker, M. R., Chowdhury, J., Shirley, N. & Little, A. The plant cell wall: a complex and dynamic structure as revealed by the responses of genes under stress conditions. *Front Plant Sci.* **7**, 984 (2016).
27. Cunningham, F. J., Goh, N. S., Demirer, G. S., Matos, J. L. & Landry, M. P. Nanoparticle-mediated delivery towards advancing plant genetic engineering. *Trends Biotechnol.* https://doi.org/10.1016/j.tibtech.2018.03.009 (2018).
28. Schwab, F. et al. Barriers, pathways and processes for uptake, translocation and accumulation of nanomaterials in plants – critical review. *Nanotoxicology* **10**, 257–278 (2016).
29. Wang, P., Lombi, E., Zhao, F.-J. & Kopittke, P. M. Nanotechnology: a new opportunity in plant sciences. *Trends Plant Sci.* **21**, 699–712 (2016).
30. Hubbard, J. D., Lui, A. & Landry, M. P. Multiscale and multidisciplinary approach to understanding nanoparticle transport in plants. *Curr. Opin. Chem. Eng.* **30**, 135–143 (2020).
31. Corredor, E. et al. Nanoparticle penetration and transport in living pumpkin plants: *in situ* subcellular identification. *BMC Plant Biol.* **9**, 45 (2009).
32. Bao, D. P., Oh, Z. G. & Chen, Z. Characterization of silver nanoparticles internalized by *Arabidopsis* plants using single particle ICP-MS analysis. *Front. Plant Sci.* https://doi.org/10.3389/fpls.2016.00032 (2016).
33. Zhang, P. et al. Shape-dependent transformation and translocation of ceria nanoparticles in cucumber plants. *Environ. Sci. Technol. Lett.* **4**, 380–385 (2017).
34. Giraldo, J. P. et al. Plant nanobionics approach to augment photosynthesis and biochemical sensing. *Nat. Mater.* **13**, 400–408 (2014).
35. Santana, I., Wu, H., Hu, P. & Giraldo, J. P. Targeted delivery of nanomaterials with chemical cargoes in plants enabled by a biorecognition motif. *Nat. Commun.* **11**, 2045 (2020).
36. Zhang, X., Servos, M. R. & Liu, J. Instantaneous and quantitative functionalization of gold nanoparticles with thiolated DNA using a pH-assisted and surfactant-free route. *J. Am. Chem. Soc.* **134**, 7266–7269 (2012).
37. Yang, G. et al. Implications of quenching-to-dequenching switch in quantitative cell uptake and biodistribution of dye-labeled nanoparticles. *Angew. Chem. Int. Ed.* **60**, 15426–15435 (2021).
38. Sattelmacher, B. The apoplast and its significance for plant mineral nutrition. *New Phytol.* **149**, 167–192 (2001).
39. Yu, M. et al. Rotation-facilitated rapid transport of nanorods in mucosal tissues. *Nano Lett.* **16**, 7176–7182 (2016).
40. Matsuoka, K., Bassham, D. C., Raikhel, N. V. & Nakamura, K. Different sensitivity to wortmannin of two vacuolar sorting signals indicates the presence of distinct sorting machineries in tobacco cells. *J. Cell Biol.* **130**, 1307–1318 (1995).
41. Elkin, S. R. et al. Ikarugamycin: a natural product inhibitor of clathrin-mediated endocytosis. *Traffic* **17**, 1139–1149 (2016).
42. Aniento, F. & Robinson, D. G. Testing for endocytosis in plants. *Protoplasma* **226**, 3–11 (2005).
43. Reynolds, G. D., Wang, C., Pan, J. & Bednarek, S. Y. Inroads into internalization: five years of endocytic exploration. *Plant Physiol.* **176**, 208–218 (2018).
44. Meister, G. & Tuschl, T. Mechanisms of gene silencing by double-stranded RNA. *Nature* **431**, 343–349 (2004).
45. Tiwari, M., Sharma, D. & Trivedi, P. K. Artificial microRNA mediated gene silencing in plants: progress and perspectives. *Plant Mol. Biol.* **86**, 1–18 (2014).
46. Bennett, M., Deikman, J., Hendrix, B. & Iandolino, A. Barriers to efficient foliar uptake of dsRNA and molecular barriers to dsRNA activity in plant cells. *Front. Plant Sci.* https://doi.org/10.3389/fpls.2020.00816 (2020).
47. Pinals, R. L., Yang, D., Lui, A., Cao, W. & Landry, M. P. Corona exchange dynamics on carbon nanotubes by multiplexed fluorescence monitoring. *J. Am. Chem. Soc.* **142**, 1254–1264 (2020).
48. Geilfus, C.-M. The pH of the apoplast: dynamic factor with functional impact under stress. *Mol. Plant* **10**, 1371–1386 (2017).
49. Chehab, E. W., Eich, E. & Braam, J. Thigmomorphogenesis: a complex plant response to mechano-stimulation. *J. Exp. Bot.* **60**, 43–56 (2009).
50. Mori, I. C. & Schroeder, J. I. Reactive oxygen species activation of plant Ca^{2+} channels. A signaling mechanism in polar growth, hormone transduction, stress signaling, and hypothetically mechanotransduction. *Plant Physiol.* **135**, 702–708 (2004).

Methods

Additional information regarding materials can be found in the Supplementary Methods section in the Supplementary Information.

Plant growth and leaf infiltration. Transgenic mGFP5 *N. benthamiana* seeds (obtained from the Staskawicz Lab, University of California (UC) Berkeley) and transgenic 16C *N. benthamiana* seeds (obtained from the Falk Lab, UC Davis and the Scholthof Lab, Texas A&M University) were germinated and grown in SunGro Sunshine LC1 Grower soil mixture in a growth chamber (740 FHLED, HiPoint; see Supplementary Note 4). The plants were grown in 10-cm pots under light-emitting-diode light (100–150 μmol $m^{-2} s^{-1}$) and a 14/10 light/dark photoperiod at 23 °C and 60% humidity. All experiments were performed on the intact leaves of 4-week-old plants, with the plants incubated in the growth chamber until the time of data collection. Young leaves (approximately 2 cm × 3 cm in size) were infiltrated using a 1 ml needleless syringe on the abaxial side of the leaves after a tiny puncture had been made with a 10 μl pipette tip.

AuNP functionalization. The AuNPs were functionalized with thiol-functionalized DNA or RNA (HS-DNA or HS-RNA, see detailed sequences in Supplementary Table 1) using a facile pH-assisted method reported previously by Zhang et al.[36]. The nanoparticles were resuspended in 0.3× PBS to obtain DNA- or RNA-functionalized AuNPs at the desired concentrations. Fluorophore-tagged AuNPs (Cy3-DNA-AuNPs) were obtained by adding a Cy3-DNA sequence complementary to the DNA on the AuNPs. The Cy3-DNA-AuNP solution was then incubated at 40 °C for 30 min, then cooled to room temperature for at least 1 h prior to use.

Nanoparticle characterization. *UV-Vis-NIR spectroscopy measurements.* Spectrophotometric measurements of the AuNPs were carried out in submicro quartz cuvettes (Cole-Parmer) with a UV-3600 Plus UV-Vis-NIR spectrophotometer (Shimadzu North America).

Dynamic light scattering measurements. DLS measurements were performed with a Zetasizer Nano ZS instrument (Malvern Analytical). Citrate-stabilized AuNPs and NA-AuNPs in 2 mM citrate and 0.3× PBS buffer, respectively, were diluted to an optical density of 1, placed in disposable cuvettes (Malvern) and positioned for DLS measurement.

Transmission electron microscopy. The structures of the AuNPs and oligonucleotide-functionalized AuNPs were examined using a JEOL 1200EX microscope, and the interactions of AuNPs with plant cells were studied with a Tecnai 12 transmission electron microscope (Berkeley Electron Microscope Lab). AuNPs were dropcast on plasma-treated Formvar carbon-coated TEM grids (Ted-Pella), then imaged at an acceleration voltage of 120 kV. To visualize siRNA on NA-AuNPs, TEM grids with dropcast NA-AuNPs were placed face down on a 2% methanolic uranyl acetate droplet for 30 s, removed and blotted with filter paper, and air-dried prior to imaging.

Quantification of DNA or siRNA on DNA-AuNPs and siRNA-AuNPs. The number of DNA and siRNA strands on each functionalized gold nanoparticle was quantified by a potassium cyanide (KCN) desorption assay previously reported by Baldock and Hutchison[51].

Tracking of AuNPs in *N. benthamiana* leaves. *Colocalization analysis of Cy3-labelled AuNPs with GFP.* Cy3-DNA-AuNP at a Cy3-DNA concentration of 400 nM were infiltrated into plant leaves and left on the benchtop at 20 °C for the desired incubation time. For samples used to investigate the nanoparticle internalization pathway, 40 μM wortmannin or 10 μM ikarugamycin solutions were infiltrated into the target leaves 30 min prior to Cy3-DNA-AuNP introduction. To prepare the infiltrated leaves for confocal imaging, a small leaf section was cut and mounted between a glass slide and #1 (130–170 μm) thickness cover slip, focusing on areas 1–3 mm radially outward from the infiltration site. Images were obtained at ×20 magnification. The same imaging parameters and quantification analyses were applied to samples imaged on different days (Supplementary Note 5).

Transmission electron microscopy. To study AuNP internalization, leaves infiltrated with AuNPs were cut into small pieces approximately 1 mm × 3 mm in size. The leaf samples were fixed using 2% glutaraldehyde and 2% Tween 20 in 0.1 M sodium cacodylate buffer (pH 7.2), then subjected to a microwave-assisted vacuum to remove air in the vacuoles. The samples were post-fixed with 1% osmium tetroxide in 0.1 M sodium cacodylate buffer (pH 7.2), dehydrated with acetone and transferred into epoxy resin for embedding. Finally, the epoxy resin-embedded samples were cut into 100-nm-thin cross-sectioned films using a Reichert-Jung Ultracut E microtome and then transferred onto bare Cu TEM grids for imaging at an acceleration voltage of 120 kV.

Synchrotron X-ray fluorescence (μXRF) imaging. WT *N. benthamiana* leaves were infiltrated with an equivalent quantity of DNA-AuNPs (0.05 mg ml^{-1} in 100 μl). Then, 24 h post-infiltration, the infiltrated leaves were harvested, cut and placed in a disposable mould (Tissue-Tek Biopsy Cryomold) in OCT (Tissue-Tek optimal cutting temperature compound). The moulds were placed in a vacuum chamber and subjected to a house vacuum for three cycles of 20-min treatment to enable OCT permeation into the leaves. Following vacuum treatment, the slices were frozen at −20 °C for 1 h. Using a CryoStar NX50 cryostat (Epredia) at −7 °C (optimized for the lowest temperature to preserve sample structural integrity with consistent results), the slices were then cut into 100-μm-thick slices, mounted onto ultrathin quartz cover slips (19 mm × 19 mm, Chemglass) and stored at −20 °C prior to beamline exposure.

μXRF images were acquired at the X-ray Fluorescence Microprobe Beamline 10.3.2 of the Advanced Light Source at Lawrence Berkeley National Laboratory[52]. Frozen samples were transported on dry ice and transferred onto a Peltier stage kept at −22 °C. All μXRF maps were recorded at an incident photon energy of 13,834.2 eV (100 eV above the Au L_2 edge) with a beam spot size of 7 μm × 7 μm using a Canberra 7-Element Silicon Drift Detector (Mirion Technologies). For Au maps, $L\alpha_1$ fluorescence emission (9,713 eV) counts were recorded. Coarse maps were first acquired with 30 μm × 30 μm pixels using 80 ms dwell time per pixel, followed by finer maps with 7 μm × 7 μm and 2 μm × 2 μm pixels using 100 ms dwell time per pixel.

Nuclease protection. siRNA-functionalized AuNPs (at concentrations corresponding to 0.2 μM siRNA) were incubated with 1.2 μg ml^{-1} RNase A at room temperature. Post-incubation, the endonuclease was inactivated with diethyl pyrocarbonate, and KCN was added to a final concentration of 18 mM to facilitate NP decomposition. After overnight incubation at 4 °C, 20 μl samples were added to 180 μl Quant-iT microRNA Assay Kit reagents (Life Technologies, Thermo Fisher Scientific) and the fluorescence was read with an Infinite M1000 PRO microplate reader (Tecan). Free siRNA controls were also measured at each timepoint. Duplicate measurements were made for each of the three experimental replicates.

In a separate experiment, DNA-AuNPs loaded with siRNA containing a 15-nucleotide complementary overhang were incubated with RNase A at room temperature. Post-incubation, the nuclease was inactivated with diethyl pyrocarbonate, and then the AuNP solution was treated with 8 M urea at 37 °C for 30 min to disrupt the interactions between DNA-AuNP and siRNA. Free siRNA controls were also measured at each timepoint. Samples were loaded and run on a 3% agarose gel prestained with SYBR Gold at 70 V for 25 min. The resulting gels were imaged using a Typhoon FLA 9500 instrument (General Electric), and gel band intensities were analysed using FIJI (https://imagej.net/software/fiji/) and GelBandFitter[53].

Tracking cargo desorption and availability from AuNP. *Anion-exchange fast protein liquid chromatography.* Leaves of WT *N. benthamiana* were infiltrated with 100 μL 0.3× PBS containing 100 nM siRNA or 10 nm siRNA-AuNSs. The infiltrated areas were harvested immediately and 10 min after infiltration and frozen in liquid nitrogen. RNA was extracted following the protocol described by Toni et al.[54] with certain modifications. We used TRIzol (Thermo Fisher Scientific) instead of phenol, and Phasemaker tubes (Thermo Fisher Scientific) were used to separate the aqueous phase.

Then, 30–40 μg of each sample was diluted with nuclease-free water to a concentration of 100–200 ng $μl^{-1}$. The diluted samples were subsequently filtered through a 0.22-μm filter before FPLC purification at 4 °C (AKTA FPLC system, HiTrap Q HP anion-exchange column (1 ml, GE Healthcare), flow rate 0.5 ml min^{-1}). Buffer A (20 mM Tris-HCl, pH 8.0) and buffer B (1.25 M NaCl + buffer A) were used for the mobile phase with a linear gradient of 0–100% buffer B over 25 column volumes. The absorbance was monitored at 280 nm and fractions were collected in 0.5 ml aliquots. For a sample of RNA, the absorbance at 280 nm was approximately 25% of the 260 nm peak (data not included in the manuscript). The fractions corresponding to the peaks identified close to the anticipated siRNA elution point were run on a 3.5% agarose gel (prestained with SYBR Gold) at 100 V for 50 min, then imaged to verify the presence of a siRNA fragment.

siRNA desorption in plant biofluid. Apoplastic fluid from mature leaves was extracted from month-old WT *N. benthamiana* plants following the protocol outlined by O'Leary et al.[55]. Plant lysate was obtained in an identical fashion to protein extraction as described in the Methods section for the western blot. The protein content of the apoplastic fluid and lysate was quantified using the Pierce 660 nm protein assay.

To test the effect of biofluid incubation across apoplastic fluid and plant lysate, 2 μg protein was incubated with 10 nm siRNA-AuNSs (at a final concentration of 300 nM siRNA) on the benchtop for 24 h, after which the AuNSs were centrifuged and the supernatant collected. The supernatant was run on a 3% agarose gel at 120 V to visualize any intact siRNA that had desorbed from the siRNA-AuNPs.

To probe the effect of apoplastic fluid incubation across various siRNA-AuNPs, 4 μg protein was incubated with siRNA-AuNPs (at a final concentration of 300 nM siRNA; note, this corresponds to different molar concentrations of gold) on the benchtop for 24 h, after which the AuNPs were centrifuged and the supernatant collected. The supernatant was run on a 3.5% agarose gel at 120 V.

Fluorescence-based dynamic exchange assay. DNA-AuNP dynamic exchange studies were completed as described previously[47]. Briefly, the same DNA-AuNP conjugation protocol was employed using 15-nm-diameter AuNPs with fluorophore-labelled, thiolated DNA (A_{10} single-stranded DNA oligomers labelled with Texas red at 5′ and thiol-modified at 3′, abbreviated TR-DNA). Fluorescent TR-DNA was tracked in various solution conditions and the displacement of DNA from the AuNP surface was monitored as an increase in TR fluorescence. For the apoplastic fluid condition, 40 µl of undiluted WT *N. benthamiana* apoplastic fluid was added to 10 µl of 25 nM TR-DNA-AuNP in 0.3× PBS solution (final concentration of 5 nM TR-DNA-AuNPs). For all other experimental conditions, 25 µl of twofold-concentrated solution was added to 25 µl of twofold-concentrated TR-DNA-AuNPs. All experiments were run in duplicate. Solutions were added by microchannel pipette into a 96-well PCR plate (hard shell PCR plates, Bio-Rad) and mixed by pipetting. The plate was sealed with an optically transparent adhesive seal (Microseal 'B' plate sealing film, Bio-Rad) and briefly spun down on a benchtop centrifuge. Fluorescence time series readings were measured with a Bio-Rad CFX96 real time qPCR system by scanning the Texas red channel every 30 s for 8 h at 22.5 °C (lid heating off).

Analysing GFP silencing in *N. benthamiana* leaves using siRNA-AuNPs. *RT–qPCR.* siRNA-AuNPs loaded with 100 nM siRNA were infiltrated into plant leaves and left on the benchtop at 20 °C for 24 h or 7 days, after which total RNA was extracted. Two-step RT–qPCR was performed to quantify GFP gene silencing with the following commercially available kits: RNeasy plant mini kit (QIAGEN) for total RNA extraction from leaves, iScript cDNA synthesis kit (Bio-Rad) to reverse transcribe total RNA into cDNA, and PowerUp SYBR green master mix (Applied Biosystems) for RT–qPCR. The target gene in our qPCR was mGFP5 (GFP transgene inserted into *N. benthamiana*), and elongation factor 1 (EF1) was chosen as the housekeeping (reference) gene[56,57]. Primers (see detailed sequences in Supplementary Table 1) for these genes (fGFP, rGFP, fEF1 and rEF1, where f represents forward, and r represents reverse) were ordered from IDT and used without further purification. An annealing temperature of 60 °C was used for RT–qPCR, which was run for 40 cycles. The RT–qPCR data were analysed by the ddCt method[58] to obtain the normalized GFP gene expression fold change with respect to the EF1 housekeeping gene and control sample. For each sample, RT–qPCR was performed as three technical replicates (three reactions from the same isolated RNA batch), and the entire experiment consisting of independent infiltrations and RNA extractions from different plants was repeated three times (three biological replicates).

Western blot. siRNA-AuNPs loaded with 100 nM siRNA were infiltrated into plant leaves and left on the benchtop at 20 °C for 3 or 7 days, after which proteins were extracted. Briefly, infiltrated leaves were cut, frozen in liquid nitrogen and ground with a pestle and mortar. Then, 350 µl lysis buffer (10 mM Tris/HCl, pH 7.5, 150 mM NaCl, 1 mM EDTA, 0.1% Nonidet P-40, 5% glycerol and 1% protease inhibitor cocktail) was added to the resulting powder, vortexed, spun down and kept on ice. All samples were incubated at 50 °C for 3 min, centrifuged at 16,000*g* for 30 min and the supernatant transferred to a new tube to obtain extracted proteins. The protein concentrations of samples were quantified using a Pierce 660 nm protein assay (Thermo Fisher), and the concentrations of proteins standardized by the addition of lysis buffer. Loading dye was added to the protein solutions, incubated at 95 °C for 10 min and centrifuged at 16,000*g* for 15 min. All sample wells were normalized to the same amount of total protein. A 4–20% Mini-PROTEAN Precast Protein Gel (Bio-Rad) was loaded with samples and run at 120 V for 60 min with a Mini-PROTEAN Tetra Cell (Bio-Rad). The gel was included in a sandwich with a methanol-activated polyvinylidene fluoride polyvinylidene fluoride membrane, placed in cold 1× Tris–glycine buffer and run at 400 mA for 60 min. To verify equal protein loading, ribulose-1,5-bisphosphate carboxylase-oxygenase band intensities were qualitatively verified by Ponceau red staining (Supplementary Note 6). After transfer, the membrane was rinsed with 1× TBST buffer three times, with 5 min between each rinse, followed by incubation for 60 min with 5% BSA in TBST and three rinses with 1× TBST, including incubations. The membrane was incubated at 4 °C on a shaker with rabbit antibody anti-GFP (1:3,000 dilution) overnight, rinsed with TBST, incubated for 60 min with goat anti-rabbit antibody (1:5,000 dilution) and rinsed with TBST. The membrane was washed briefly in MilliQ water, exposed to Pierce ECL western blotting substrate (Thermo Fisher Scientific) and immediately imaged. Three biological replicates were collected, and band intensity analyses performed on each.

Probing the response of AuNP infiltration into *N. benthamiana* by RT–qPCR. A total of 13 genes associated with various types of stress responses were selected to understand the impact of AuNP infiltration into *N. benthamiana*. First, 16C *N. benthamiana* leaves were infiltrated with buffer, citrate-stabilized 10 nm AuNS (same AuNS concentration as siRNA-AuNSs) or 10 nm siRNA-AuNSs (siRNA concentration of 100 nM). The leaves were harvested immediately and 24 h post-infiltration, frozen in liquid nitrogen and lysed with a bead beater. Subsequent RNA extraction, cDNA synthesis and RT–qPCR were performed as previously described. For the *NbrbohB* analysis performed using 10 nm siRNA-AuNSs and siRNA-AuNRs, we used mGFP5 *N. benthamiana* leaves infiltrated with buffer, free siRNA or siRNA-AuNP (corresponding to 100 nM siRNA) and harvested tissue at 1 dpi for downstream RT–qPCR analysis.

Statistics and data analysis. Three biological replicates for each timepoint were used in confocal colocalization, RT–qPCR and western blot experiments. A one-way ANOVA was performed for the aforementioned experiments and a two-way ANOVA was used for the confocal colocalization experiment with endocytosis inhibitors. GraphPad Prism software was used in statistical analyses and data visualization. For more information, refer to the Supplementary Statistics and Data Analysis section in the Supplementary Information.

Data availability

The key datasets generated and analysed during this study are available in the Zenodo repository with the identifier https://doi.org/10.5281/zenodo.5515736. Additional data related to this study are available from the corresponding author upon reasonable request. Correspondence and requests for materials should be addressed to M.P.L.

References

51. Baldock, B. L. & Hutchison, J. E. UV–visible spectroscopy-based quantification of unlabeled DNA bound to gold nanoparticles. *Anal. Chem.* **88**, 12072–12080 (2016).
52. Marcus, M. A. et al. Beamline 10.3.2 at ALS: a hard X-ray microprobe for environmental and materials sciences. *J. Synchrotron Radiat.* **11**, 239–247 (2004).
53. Mitov, M. I., Greaser, M. L. & Campbell, K. S. GelBandFitter – a computer program for analysis of closely spaced electrophoretic and immunoblotted bands. *Electrophoresis* **30**, 848–851 (2009).
54. Toni, L. S. et al. Optimization of phenol-chloroform RNA extraction. *MethodsX* **5**, 599–608 (2018).
55. O'Leary, B. M., Rico, A., McCraw, S., Fones, H. N. & Preston, G. M. The infiltration-centrifugation technique for extraction of apoplastic fluid from plant leaves using *Phaseolus vulgaris* as an example. *J. Vis. Exp.* https://doi.org/10.3791/52113 (2014).
56. Nicot, N., Hausman, J.-F., Hoffmann, L. & Evers, D. Housekeeping gene selection for real-time RT-PCR normalization in potato during biotic and abiotic stress. *J. Exp. Bot.* **56**, 2907–2914 (2005).
57. Selvakesavan, R. K. & Franklin, G. Nanoparticles affect the expression stability of housekeeping genes in plant cells. *Nanotechnol., Sci. Appl.* **13**, 77–88 (2020).
58. Schmittgen, T. D. & Livak, K. J. Analyzing real-time PCR data by the comparative CT method. *Nat. Protoc.* **3**, 1101–1108 (2008).

Acknowledgements

We thank the Staskawicz Lab (University of California, Berkeley) for sharing mGFP *N. benthamiana* seeds, the Falk Lab (University of California, Davis) and the Scholthof Lab (Texas A&M University) for their provision of line 16C *N. benthamiana* seeds, and M.-J. Cho (Innovative Genomics Institute, Berkeley) for his assistance in *N. benthamiana* growth. We thank A. Avellan and A. Landolino for helpful discussions regarding sample preparation, and T. Cheng for assistance with performing autocorrelation function calculations. The authors recognize that majority of this work was performed on the territory of Huichin, the unceded land of the Ohlone people. We acknowledge support of a Burroughs Wellcome Fund Career Award at the Scientific Interface (CASI), a Stanley Fahn PDF Junior Faculty Grant (award no. PF-JFA-1760), a Bakar Award, a Beckman Foundation Young Investigator Award, a USDA AFRI award, a USDA NIFA award and a Foundation for Food and Agriculture Research (FFAR) New Innovator Award (M.P.L.). This research was supported by the Office of Science (BER), US Department of Energy (DOE; grant no. DE-SC0020366, M.P.L.). M.P.L. is a Chan Zuckerberg Biohub investigator. N.S.G. is supported by a FFAR Fellowship. J.W.W. is a recipient of the National Science Foundation Graduate Research Fellowship. H.Z. acknowledges the start-up funding from Jinan University. S.-J.P. acknowledges support from the LG Yonam Foundation and National Research Foundation of Korea (grant no. NRF-2017R1A5A1015365). We acknowledge the support of UC Berkeley CRL Molecular Imaging Center, the UC Berkeley Electron Microscopy Lab and the Innovative Genomics Institute. We thank the ALS Diffraction and Imaging Program for support. This research used resources of the Advanced Light Source, a US DOE Office of Science User Facility (contract no. DE-AC02-05CH11231). We acknowledge the use of Servier Medical Art elements (http://smart.servier.com), licensed under a Creative Commons Attribution 3.0 Unported Licence.

Author contributions

H.Z. and N.S.G. conceived the project, designed the study and wrote the manuscript. H.Z. and N.S.G. performed the majority of experiments and data analysis. J.W.W., G.S.D. and E.G.-G contributed key input and advanced project direction. J.W.W. performed confocal microscopy on Cy3-DNA-AuNR3 samples. R.L.P. designed,

executed and analysed the dynamic exchange experiments. E.G.-G., A.D.R.F. and R.Z. performed the anion-exchange FPLC experiments. S.C.F. performed the μXRF measurements and processed the data. B.Z. performed the assembly of AuNR3. S.B. performed the initial experiments, verifying project feasibility. All authors edited and commented on the manuscript and gave their approval of the final version.

Competing interests

The authors declare no competing interests.

Additional information

Supplementary information The online version contains supplementary material available at https://doi.org/10.1038/s41565-021-01018-8.

Correspondence and requests for materials should be addressed to Markita P. Landry.

Peer review information *Nature Nanotechnology* thanks Mohamed El-Shetehy, Shadi Rahimi and the other, anonymous, reviewer(s) for their contribution to the peer review of this work.

Reprints and permissions information is available at www.nature.com/reprints.